Observation and Prediction of Three-Dimensional Morphology at a High Energy Macrotidal Beach

Christopher Stokes*, Mark Davidson, Paul Russell

School of Marine Science and Engineering, University of Plymouth, Drake Circus, Plymouth, PL4 8AA, UK.

Christopher.Stokes@plymouth.ac.uk

M.Davidson@plymouth.ac.uk

P.Russell@plymouth.ac.uk

*Corresponding author, tel.: +44 (0)1752 586102, email: Christopher.Stokes@plymouth.ac.uk, post: School of Marine Science and Engineering, University of Plymouth, Plymouth, PL4 8AA, UK.

Abstract

Three-dimensional beach features such as crescentic sandbars and rip channels influence beach response to, and recovery from, storm waves, as well as significantly affecting the safety and amenity provided by the surf-zone for beach water-users. In this contribution temporal variations in subtidal and intertidal beach three-dimensionality are observed at a high-energy macrotidal beach, and a simple equilibrium model is developed to predict the changes over multi-year timescales. A dataset of 5.5 years of quasi-weekly bar measurements, and quasi-monthly intertidal surveys from Perranporth beach (Cornwall, UK) were used to quantify seasonal to inter-annual changes in three-dimensionality. The three-dimensionality of the outer bar displayed significant annual periodicity, with annual minima and maxima occurring in winter and spring, respectively. The lower intertidal beach displayed a similar periodicity, but developed three-dimensionality 1-4 months before the

outer bar. The model predicts increases or decreases in the scale of three-dimensional features by examining the disparity between instantaneous wave conditions and a temporally varying equilibrium wave condition. A tidally-modulated wave power term determines the rate of morphological change. Negative feedback was found to be an important process governing the changes in three-dimensionality; while free morphological behaviour may drive three-dimensional growth, negative feedback exerts stability in the system, making it inherently predictable using a temporally varying equilibrium value. The model explained 42% and 61% of the overall variability in outer bar and lower beach three-dimensionality, respectively. It skilfully predicted changes outside the training data range, during the most energetic 8-week period of waves measured in the last 65 years off SW England, in winter 2013/14. The model outperformed a simple baseline model (a linear fit), as well as a comparable linearized feedback model from the literature, providing the first long-term (multi-year) predictions of seasonal to inter-annual beach three-dimensionality for a macrotidal beach.

Keywords: Three-dimensional, sandbar, morphology, equilibrium, behavioural, macrotidal

1. Introduction

1.1 Background and rationale

Much of our conceptual understanding about the variability of beach morphology comes from sequential models developed for single-barred microtidal beaches in Australia (Short, 1979; Wright and Short, 1984; Wright *et al.*, 1985). Through extensive field observations made over a number of years, Wright and Short (1984) reduced the natural continuum of beach forms into a sequence of 6 discrete states. The end-members of the model have a shallow gradient in the Dissipative (D) extreme, or a steep gradient in the Reflective (R) extreme, both of which consist of a planar beach face with little alongshore variability. The intermediate stages (Longshore Bar and Trough - LBT, Rhythmic Bar and Beach - RBB, Transverse Bar and Rip - TBR, Low Tide Terrace - LTT) are typified by

greatly increased alongshore variability in the form of rip channels, and crescentic bar formations. The general applicability of this sequence has subsequently been verified at other sites and extended to include beaches with meso- and macro-tidal range (Short, 1991; Masselink and Short, 1993; Masselink and Hegge, 1995; Scott *et al.*, 2011; Masselink *et al.*, 2014), double or multi-bar systems (Short, 1992; Short and Aagaard, 1993; Castelle *et al.*, 2007; Scott *et al.*, 2011), and beaches with dominant headlands or geological features (Short, 1996; Castelle and Coco, 2012; Loureiro *et al.*, 2012). Although the intermediate beach forms observed in the different studies vary slightly, they all feature alongshore non-uniformities such as rip channels and crescentic bars, collectively referred to as three-dimensional (3D) morphology (see Fig. 1 for example images).

Beach morphology often becomes 3D during the recovery period following energetic waves, when the straightened, offshore bar(s) migrates back toward shore unevenly under the action of accretive, low-steepness waves (Short, 1979; Wright and Short, 1984; Lippmann and Holman, 1990; Poate *et al.*, 2014). The result is a sinuous, crescentic bar which can either be rhythmic in form, or a range of wavelengths (from 150 m – 2 km) and cross-shore amplitudes (from 5 – 80 m) can occur (Van Enckevort *et al.*, 2004). Under sustained accretive conditions the shoreward bar horns will eventually weld to the shore, resulting in the highly 3D TBR beach state. The final states in the 'downstate' sequence feature diminishing three-dimensionality, and a bar that is close to shore (LTT and R). The landward return of sediment during this downstate sequence forms an important mechanism for beach recovery following erosive, 'upstate' conditions. Conversely the presence of 3D features such as cusps and rip channels during a storm can potentially allow erosive swashes to reach further landward and undercut the dune foot (Thornton *et al.*, 2007). 3D morphology therefore heavily influences a beach's response to, and recovery from, storm waves.

3D features also significantly affect the safety and amenity provided by the surf-zone for beach water-users. The alongshore varying morphology causes localised refraction and breaking; while these factors improve the amenity provided by waves for popular recreational activities such as

surfing (Mead and Black, 2001a; Mead and Black, 2001b; Scarfe et al., 2009), they also influence the type and strength of surf-zone currents (Bowen, 1969; Ranasinghe *et al.*, 2004). Rip channels allow water set-up by wave breaking to funnel back out to sea in concentrated offshore flows (Fig. 1) which can take water-users from the shallows out into deeper water (MacMahan *et al.*, 2006; Austin *et al.*, 2010). As a result rip currents are the largest cause of surf-zone rescues and fatalities globally (Scott *et al.*, 2008; MacMahan *et al.*, 2011; Scott *et al.*, 2011; Brighton *et al.*, 2013). In the UK 90% of rip incidents occur during the highly 3D intermediate Low Tide Bar-Rip (LTBR) and LTT with rip (LTT+R) beach states (Scott *et al.*, 2008), which are analogous to the TBR and LTT states.

1.2 Approaches to modelling three-dimensional morphology

Process-based models have shown that horizontal wave-driven circulation in the nearshore contributes to the growth of 3D morphology through positive feedback between the developing morphology and local hydrodynamics, termed bed-surf coupling (Falqués *et al.*, 2000; Caballeria *et al.*, 2002; Caballeria *et al.*, 2003a; Caballeria *et al.*, 2003b; Ranasinghe *et al.*, 2004). In the case of subtidal bars, this process starts with waves breaking preferentially over the shallowest bar sections. The dispersion of energy and gradient of the beach decelerates the shoreward flowing water, promoting a decreasing sediment flux and sand deposition directly shoreward of the bar, further reducing the water depth and enhancing wave breaking in that region (Falqués *et al.*, 2000; Falqués *et al.*, 2008). The water set-up by the breakers locally increases hydrostatic pressure and forces an alongshore flow away from the region of breaking. These flows converge at points between the shallow regions of wave breaking, and return seaward over the deeper portions of the sandbar crest, creating horizontal circulation (Fig. 1) (Falqués *et al.*, 2000; Ranasinghe *et al.*, 2004). The offshore-directed return flows are coupled with increasing sediment fluxes and sand erosion, enhancing the depth of the channels between the horns. Eventually the developing morphology begins to hinder the sediment transport and the initial positive feedback diminishes as equilibrium is approached (Smit *et al.*, 2008). This ‘negative feedback’ has been shown to play an important role in controlling free morphological behaviour, making the system inherently predictable (Plant *et al.*, 2006).

Behavioural models provide an alternative approach to process-based modelling of 3D morphology. Although sometimes criticized for consisting of incomplete physical representations (Splinter *et al.*, 2011; Van de Lageweg *et al.*, 2013) or being overly dependent on tuning parameters (Ruessink *et al.*, 2013), behavioural models are often capable of explaining substantial amounts of data variance and accurately forecasting large-scale beach changes over multiyear timescales (e.g. Plant *et al.*, 1999; Yates *et al.*, 2009; Davidson *et al.*, 2010; Splinter *et al.*, 2011; Davidson *et al.*, 2013a), which is presently unachievable using process-based models. Wright *et al*. (1985) proposed a behavioural beach state model based on the assumption that state changes occur when instantaneous wave conditions differ from the conditions associated with zero change for each state, termed the disequilibrium stress, $\Delta\Omega$:

$$\Delta\Omega = \Omega - \Omega_{\mathrm{eq}} \tag{1}$$

where Ω and Ω_{eq} are the instantaneous and equilibrium dimensionless fall velocity respectively (Gourlay, 1968; Dean, 1973):

$$\Omega = \mathrm{H_b} / \overline{\mathrm{W}}_{\mathrm{s}} \mathrm{T_p} \tag{2}$$

$\mathrm{H_b}$ is significant wave height ($\mathrm{H_s}$) at breaking, $\overline{\mathrm{W}}_{\mathrm{s}}$ is the mean sediment fall velocity, and $\mathrm{T_p}$ is the peak wave period. Large departures from equilibrium (large $\Delta\Omega$) represent an increased potential for change, and upstate and downstate changes occur under positive and negative disequilibrium, respectively. As instantaneous conditions approach the equilibrium condition ($\Omega \rightarrow \Omega_{\mathrm{eq}}$) the morphological change appropriately reduces to zero. Although successful predictions of beach state were not achieved by Wright *et al*. (1985), their approach recognizes the importance of negative feedback in maintaining system stability, and the concept may therefore be suited to predicting beach three-dimensionality. Disequilibrium stress has since been used in adapted forms to predict cross-shore shoreline (Yates *et al.*, 2009; Davidson *et al.*, 2010; Yates *et al.*, 2011; Davidson *et al.*, 2013a; Castelle *et al.*, 2014; Splinter *et al.*, 2014) and barline (Plant *et al.*, 1999; Masselink *et al.*,

2014) migration under varying waves, but is yet to be applied to the prediction of alongshore non-uniform changes. Other attempts to behaviourally model three-dimensionality have either been restricted to single storm cycles (Plant *et al.*, 2006) or have included relatively complex sediment transport parameterisations, with limited predictive improvement (Splinter *et al.*, 2011).

1.3 Aims

This study aims to investigate the temporal variability of seasonal to inter-annual, subtidal and intertidal beach three-dimensionality at a high energy, macrotidal beach (Perranporth, Cornwall, UK). A morphological data set consisting of 5.5 years of monthly intertidal surveys and quasi-daily Argus barline observations presents an opportunity to apply disequilibrium stress to the prediction of subtidal and intertidal three-dimensionality for the first time. Furthermore this will be the first attempt to model multi-year changes in three-dimensionality at a macrotidal beach.

Figure 1. Examples of three-dimensional beach morphology from the microtidal New South Wales coast, Australia (Price *et al.*, 2014), meso-macrotidal Aquatanian coast, France (Castelle *et al.*, 2007), and macrotidal North Cornwall coast, England (left to right panels respectively). Yellow arrows demonstrate typical wave-driven horizontal cell circulation with seaward directed rip current component.

2. Methods

2.1 Study area

Perranporth (PPT) beach on the North West coast of Cornwall, UK (Fig. 2) is fully exposed to the dominant westerly wave approach, receiving an energetic wave climate of Atlantic swell and locally generated wind seas (Davidson *et al.*, 1997). The directional wave rider buoy located just offshore in approximately 15 m water depth (upwards triangle, Fig. 2) measured mean and maximum significant wave heights, $\mathrm{H_s}$, of 1.6 m and 7.2 m, respectively, and a mean peak period, $\mathrm{T_p}$, and direction, θ_{p}, of 10.6 s and 283°, respectively, between January 2007 and May 2014. The region is macrotidal, with mean neap and spring tide ranges of 3.1 m and 6.1 m, respectively. The beach is 3.4 km long with a cross-shore extent of approximately 500 m at spring low tide. Devonian hard rock cliffs and steep vegetated dunes surround the beach. The sediment is composed of medium quartz sand with a median grain size $\mathrm{D_{50}}$ (mean fall velocity $\overline{\mathrm{W_s}}$) of 0.35 mm (0.04 m s^{-1}) (Poate *et al.*, 2014). The lower beach gradient is shallow ($tan\beta \approx 0.012$), but compared to the subdued (<1 m vertical range) and alongshore-uniform morphology that characterise the upper beach, the region below mean-low-water-neap (MLWN) is highly dynamic (2 m vertical range), and the double bar system regularly exhibits pronounced crescentic bar and rip features (see example in Fig. 3) (Poate, 2011; Austin *et al.*, 2013; Masselink *et al.*, 2014).

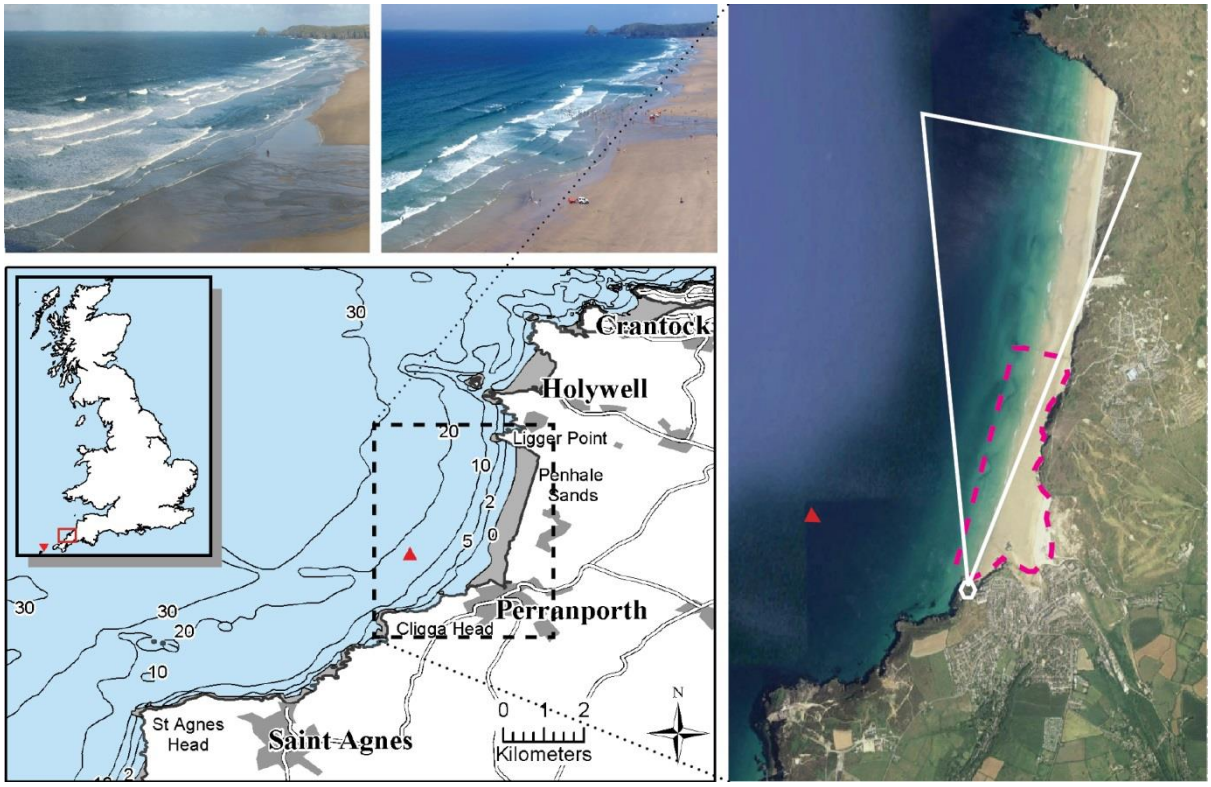

Figure 2. Map of study site and example morphology. The bottom left panel shows the geographic location and bathymetry of Perranporth beach. The right panel shows the location (white octagon) and field of view (large white triangle) of the Argus camera, and the typical intertidal survey extents (dashed magenta region). The position of the nearshore wave buoy is shown in the bottom left and right panels as an upwards pointing triangle, while the deep-water wave buoy is shown in the inset map as a downwards pointing triangle. The top left and top middle panels show examples of 2D (without rips) and 3D (with rips) morphology, taken from the Argus station vantage point in August and November 2008, respectively.

2.2 Observation of beach three-dimensionality

2.2.1 Video data

An elevated Argus video camera located at the southern end of the beach (Fig. 2) collected time exposure (timex) images of the lower intertidal and subtidal regions between September 2008 and April 2014. As a result of the preferential breaking of waves over the shallow bar crests, foam is often visible on the water surface at the position of the sandbars, creating conspicuous bands of high pixel intensity that reveal the position of the underlying bars (Lippmann and Holman, 1989). A barline intensity mapping tool (Pape *et al.*, 2007) was used to detect the inner and outer bar crest

positions by the alongshore tracking of the intensity maxima within the surf zone (Fig. 3). The barlines were measured at 1 m intervals, between -1700 m and -200 m alongshore. The detected barline positions can be artificially shifted due to tide and wave conditions (Kingston *et al.*, 2000; Van Enckevort and Ruessink, 2001). To minimize tidal shifting, a single low tide image was selected for each day (Van Enckevort and Ruessink, 2001), and to minimize the combined effects of a large tide range and large waves, or a small tide range with small waves, images were also constrained by the Hydrodynamic Forcing Index (Almar *et al.*, 2010):

$$\mathrm{HFI} = \frac{\mathrm{H_s}}{\mathrm{d_{min}}} \tag{3}$$

where $\mathrm{H_s}$ is averaged over a tidal cycle and $\mathrm{d_{min}}$ is the lowest water level above the lowest astronomical tide experienced during a tidal cycle. To maximise clear breaking over the bars, only images collected within the following hydrodynamic constraints were used:

$$0.5\ \mathrm{m} < \mathrm{H_s} < 2\ \mathrm{m}$$

$$0.9 < \mathrm{HFI} < 2$$

Images were also unavailable during poor light and weather conditions, or occasionally due to technical issues with the camera system. Of the 2067 days of the study period 254 usable images were obtained, with a minimum, mean and maximum interval of 1, 8 and 74 days, respectively.

2.2.2 Topographic surveys

Topographic surveys were conducted using an RTK-GPS system mounted on an all-terrain vehicle (ATV) each month between October 2008 and April 2014. The surveys were conducted around low tide during the largest spring tide of each month, to maximise beach coverage. Typical survey extents are shown in Fig. 2. A total of 64 monthly surveys were conducted, with a minimum, mean and maximum interval of 16, 32 and 73 days respectively. The collected topographic data were used to generate digital elevation maps (DEM's), which were converted from OSGB36 coordinates by

rotation and translation to the same local grid as used by the Argus camera system (Fig. 3). The data were gridded at 20 m resolution in both the alongshore and cross-shore directions with a quadratic loess interpolation scheme (Plant *et al.*, 2002).

2.2.3 Parameterisation of three-dimensionality

To objectively quantify the three-dimensionality of the subtidal bars, the standard deviation, α, about the alongshore averaged cross-shore position, X_c, of the barlines was measured in keeping with previous studies of barline variability (Plant *et al.*, 2006; Splinter *et al.*, 2011). To obtain a single representative measure of α at the lower beach, contours were extracted from each DEM every 0.2 m between +0.2 m Ordnance Datum Newlyn (ODN) and -2.4 m ODN (between -1100 m and 200 m alongshore, thin dashed lines in Fig. 3), and the mean of the highest 1/3rd of α values was used. Short contours covering less than 2/3rd of the alongshore length of the survey area were omitted to avoid erroneous α values. It is recognised that across flat, non-sloping sections this parameter could incorrectly yield large values of α. As the lower beach region at Perranporth was either planar and gently sloping, or exhibited 3D features in this data set, this was not deemed to be an issue and α was used in the form described above for consistency with the barline measurements. At sites which exhibit flat profile sections, other computations of α should be considered however. The MLWN contour (thick dashed line in Fig. 3) was chosen to represent the cross-shore position (X_c) of the lower beach. Before calculating α the barlines and contours were linearly de-trended, then band-pass filtered between 25 and 1000 m. For reference, 0 m ODN is approximately Mean Sea Level (MSL) at this beach.

To estimate measurement errors Argus detected barlines were compared to residual barlines (Masselink *et al.*, 2014) from 10 bathymetric surveys. The root-mean-square measurement errors, ΔX_c and $\Delta\alpha$, were 13.82 m and 4.78 m, respectively, at the outer bar. The inner bar data were deemed to have excessively large $\Delta\alpha$ (16.55 m), which is thought to be due to saturation of the inner surf-zone at low tide when the Argus images were collected. As such the inner bar data are not

included in this study. The measurement error from the intertidal contours was conservatively estimated by summing the accuracy of the RTK-GPS equipment (+/- 0.03 m) and maximum interpolation error (+/- 0.05 m), resulting in ΔX_c and $\Delta\alpha$ of 0.08 m and 0.16 m, respectively. As seasonal and inter-annual changes are of primary interest, the α and X_c time series were low-pass filtered using a frequency domain Fourier filter with 1/42 days cut off, chosen to be sufficiently longer than the timescale of individual storms yet shorter than an individual season. Examples of α and X_c measured at the lower beach, and outer bar are shown in Fig. 3. The data time series are plotted in Fig. 5, where vertical dotted lines indicate the data measured in Fig. 3.

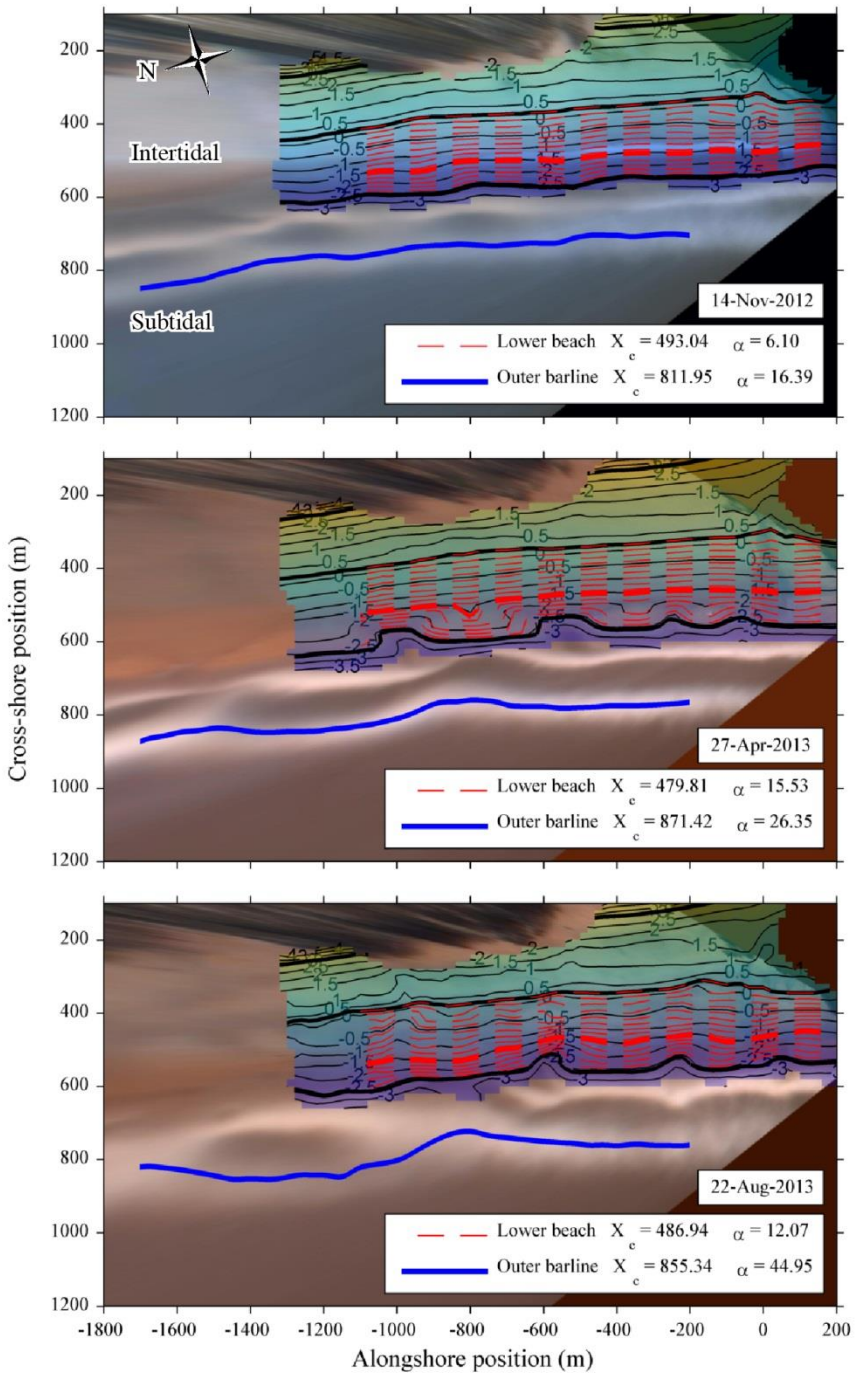

Figure 3. Combined topographic survey data (semi-transparent contour plots) and rectified timex images from Perranporth beach, demonstrating seasonal changes in three-dimensionality. The thin dashed lines and thick subtidal line in each plot show the lower beach contours and outer barline respectively, used to determine the three-dimensionality, α, of the intertidal and subtidal regions respectively. The thick dashed line shows the MLWN contour used to represent the cross-shore position of the lower beach. The solid contour lines show elevation (m) above ODN, and the thick lines indicate (top to bottom) Mean-High-Water-Spring, Mean-Sea-Level and Mean-Low-Water-Spring, respectively.

2.3 Wave and tide data

Wave data were provided by a nearshore Datawell Waverider III buoy (Fig. 2), moored at a water depth of approximately 15 m. The half hourly wave statistics were used to calculate daily mean values of significant wave height, H_s, peak wave period, T_p, and peak wave direction, θ_p. Occasional gaps exist in the wave series; daily mean parameters were calculated for days with at least 75% of measurements present, leaving 203 days (7.6 %) over the period of interest (2007 – 2014) with missing measurements. These gaps were filled using adjusted wave data from the Sevenstones lightship, located in deep water approximately 70 km south-west of PPT (Fig. 2). A linear fit between the PPT and Sevenstones data was used to adjust the deep water data to approximate nearshore conditions. Correlation between the available PPT measurements and the concurrent adjusted Sevenstones measurements was high (r = 0.92 and 0.81, RMSE = 0.36 m and 1.68 s, for H_s and T_p, respectively). Remaining H_s and T_p data gaps (16 days, 0.6 %) and all gaps in θ_p (203 days, 7.6 %) were filled using time-series mean values. H_b was calculated from linear theory using the formula of Larson *et al*. (2010), and depth-limited breaking was imposed using a commonly applied depth breaker ratio of 0.78 (Sverdrup and Munk, 1946). A continuous prediction of tidal elevation over the period of interest was generated from pressure transducer data from a 3 month deployment (Poate, 2011). Example wave and tide data are shown in Fig. 4.

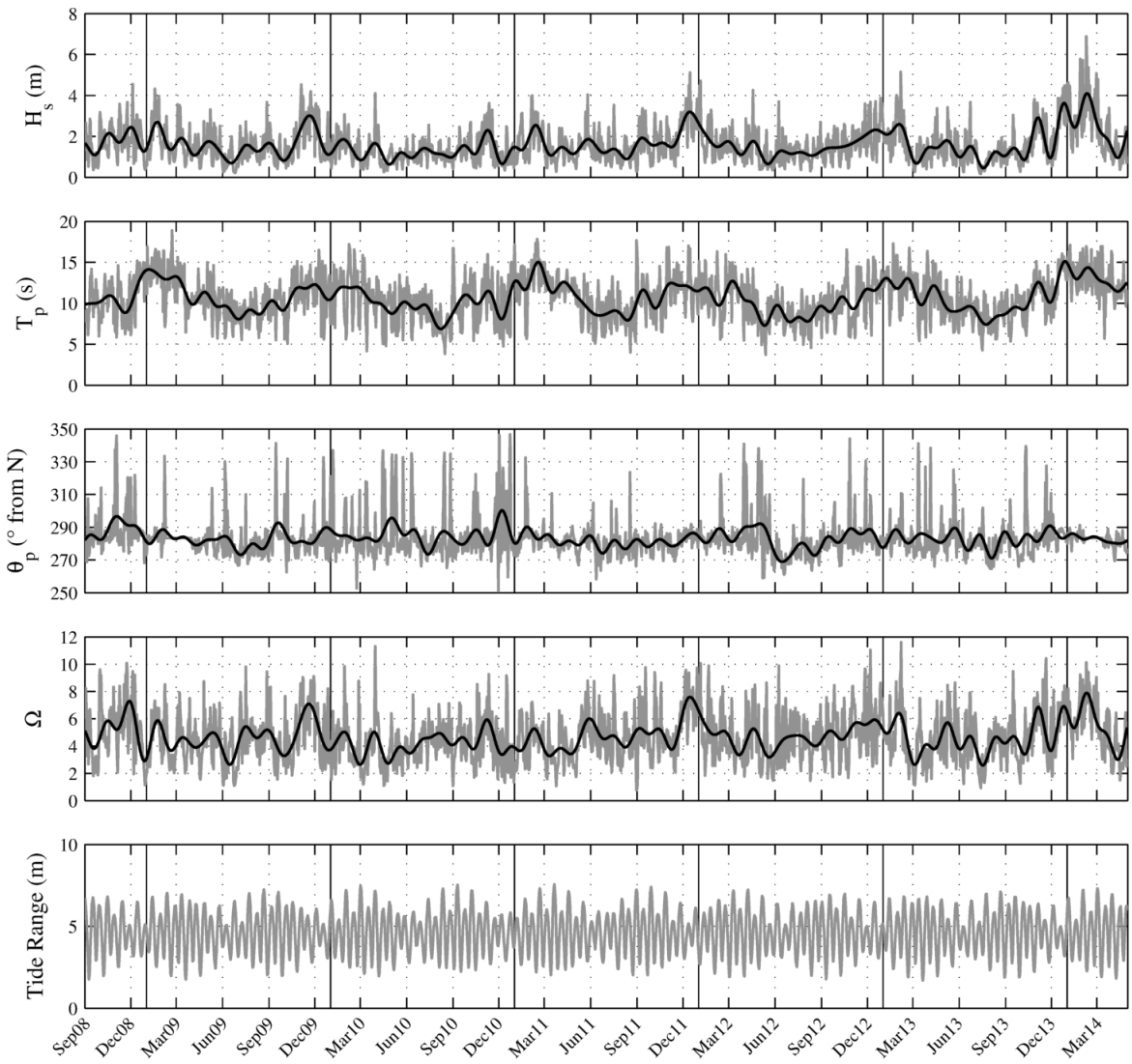

Figure 4. Wave and tide measurements over the study period. H_s, T_p and θ_p are plotted as measured by the PPT wave buoy in ~15 m depth. Thin lines are daily average values, thick lines show the seasonal signal, after low-pass filtering with a 1/42 day cut-off. Vertical lines indicate the start of each year.

2.4 Modelling beach three-dimensionality

2.4.1 DST13 model.

Davidson *et al*. (2010; 2013a; 2013b) applied the concept of disequilibrium stress to the prediction of cross-shore shoreline position at two Australian beaches; their formula are developed here to better suit the prediction of three-dimensionality (α). The adapted model predicts the rate of change in α, taking the following form (herein referred to as DST13):

$$\frac{d\alpha}{dt} = b + c(\mathrm{F}^{+} + r\mathrm{F}^{-}) \quad (4)$$

The forcing term F is defined as the product of the incident wave power raised to the 0.5 exponent, $\mathrm{P}^{0.5}$, and the normalised disequilibrium ($\Delta\Omega$):

$$\mathrm{F} = \mathrm{P}^{0.5}\frac{\Delta\Omega}{\sigma_{\Delta\Omega}} \quad (5)$$

$\Delta\Omega$ controls the direction of beach change (2D to 3D or 3D to 2D) and for convenience positive values are associated with increasing three-dimensionality by changing the sign of Eq. (1) (therefore $\Delta\Omega = \Omega_{\mathrm{eq}} - \Omega$). Following Splinter *et al*. (2014) $\Delta\Omega$ is normalised by its standard deviation (denoted $\sigma_{\Delta\Omega}$ in Eq. 5), so that the rate of change in α is predominantly controlled by the rate parameter, c, and the wave power ($\mathrm{P}^{0.5}$), rather than the magnitude of $\Delta\Omega$. Ω_{eq} is determined from weighted antecedent values of Ω, and is highly dependent on a memory decay parameter ϕ, which determines the number of days, i, prior to the present time at which the weighting function has dropped to 10%:

$$\Omega_{\mathrm{eq}} = \left[\sum_{\mathrm{i}=1}^{2\phi} 10^{-\mathrm{i}/\phi}\right]^{-1} \sum_{\mathrm{i}=1}^{2\phi} \Omega_{\mathrm{i}} 10^{-\mathrm{i}/\phi} \quad (6)$$

Low ϕ values (<30 days) indicate a short, storm dominated response time, whereas large values (>100 days) indicate that variations from the long-term mean conditions cause changes in α (Davidson *et al.*, 2013a). Example weightings are discussed in section 4.2.

Water depth over the bar crest, and by association tidal range, have been recognised as important modulators of wave driven horizontal circulation and therefore the development of 3D morphology (Caballeria *et al.*, 2003a; Caballeria *et al.*, 2003b; Almar *et al.*, 2010; Austin *et al.*, 2013). Austin *et al.* (2013) for example found that rip currents at Perranporth reached maximum velocities around spring low tide, which is likely to enhance the sediment transport potential. The forcing term F is therefore modified to include the combined effects of a large tidal range and high wave power by

adapting a previously used parameter, the normalised wave power, $P\eta_o$ (Morris *et al.*, 2001; Loureiro *et al.*, 2012):

$$P\eta_o = P^{0.5}(\eta_{dtr}/\eta_{str}) \tag{7}$$

where η_{dtr} and η_{str} are the maximum daily and spring tide ranges respectively. When the tide range approaches its overall (spring tide) maximum, the ratio on the right-hand side approaches unity and the normalised wave power is maximised. Conversely during neap tides the ratio drops to around ½, reducing the normalised wave power by half. In initial tests, inclusion of this tidally modulated power term made little difference to the lower beach predictions (R^2 was 0.61 in both cases), but significantly improved model skill at the outer bar, increasing R^2 from 0.32 to 0.42. The Relative Tide Range parameter (Masselink and Short, 1993) and HFI parameter (Almar *et al.*, 2010) were also tested but did not yield comparable model improvements.

Recognising that increasing and decreasing three-dimensionality are caused by different physical processes, the forcing term F is broken into positive and negative elements in Eq. (4):

$$F = P\eta_o \frac{\Delta\Omega}{\sigma\Delta\Omega} \tag{8}$$

$$F^+ = P\eta_o \frac{\Delta\Omega}{\sigma\Delta\Omega} \qquad (\text{when } \Omega < \Omega_{eq}) \tag{8a}$$

$$F^- = P\eta_o \frac{\Delta\Omega}{\sigma\Delta\Omega} \qquad (\text{when } \Omega > \Omega_{eq}) \tag{8b}$$

The relative weighting of F^+ and F^- are determined by the ratio term r in Eq. (4); this is calculated from the wave data and is therefore not considered a 'model free' parameter. r describes the relative efficiency of positive and negative disequilibria in altering the beach three-dimensionality, and long-term equilibrium is maintained if:

$$r = \left|\frac{\sum_{i=0}^{N} \hat{F}_i^+}{\sum_{i=0}^{N} \hat{F}_i^-}\right| \tag{9}$$

N is the length of the time series, and the triangular over-bar represents a numerical operation that removes any linear trend in F, but retains the time-series mean. As negative disequilibrium (e.g. storms) often has higher associated wave power, a strong tendency towards beach straightening would be predicted if only F was considered. Instead r is determined such that zero trend in the forcing results in zero trend in α, and therefore the term $(\mathrm{F}^{+} + r\mathrm{F}^{-})$ only contributes to a predicted trend if one exists in the wave forcing series. Any trend in α not explained by trends in the wave series is handled (albeit crudely) by the trend term b in Eq. (4).

To predict values of α at times t, F and r are computed from the wave data and Eq. (4) is numerically integrated with respect to time, yielding the final model equation:

$$\alpha(t) = \mathrm{a} + bt + c\int_0^{\mathrm{t}}(\mathrm{F}^{+} + r\mathrm{F}^{-})\,dt \tag{10}$$

where a is an offset that deals with non-zero mean values of α. Eq. (10) is regressed against observed values of $\alpha(\mathrm{t})$ using a least squares method to optimize the coefficients *b, c* and offset a. The optimal ϕ value is determined iteratively by changing ϕ from 1 to 1000 days, each time regressing the model against calibration data, and finally using the ϕ that yields the greatest R^2.

2.4.2 PHH06 model

The predictions of the DST13 model will be compared to an existing behavioural model. Recognising the coupling between X_c and α, Plant *et al*. (2006) proposed a linearized feedback model that assumes that rates of change in X_c and α are dependent on their instantaneous values as well as the squared instantaneous wave height, $\mathrm{H_b^2}$. The model involves two coupled differential equations and by necessity simultaneously estimates both X_c and α, taking the following combined form (herein referred to as PHH06):

$$\begin{bmatrix}\dot{X}_c\\ \dot{\alpha}\end{bmatrix} = A\begin{bmatrix}X_c\\ \alpha\end{bmatrix} + B\begin{bmatrix}1\\ \mathrm{H_b^2}\end{bmatrix} \tag{11}$$

where, for brevity, $\dot{X}_c$ and $\dot{a}$ denote rates of change. X_c or α are predicted by integrating all terms in Eq. (11) with respect to time, then separately optimising the [2 x 2] coefficient matrices (A and B) through least squares regression against observations. Full details are given in the original text (Plant *et al.*, 2006).

2.4.3 Assessment of model skill

Four objective measures of the models' predictive ability are assessed, namely:

1. The squared correlation, R^2, between the model predictions, x_m, and measured data, x.
2. The root-mean-squared error (RMSE) between x_m and x.
3. The Brier Skill Score, BSS, which quantifies the improvement that the model predictions provide over that of a pre-defined benchmark model, x_b (in this case a linear fit to the data). BSS also considers the estimated measurement error in the data, Δx (m), and is therefore deemed highly suited to assessment of morphological models (Sutherland *et al.*, 2004):

$$BSS = 1 - \left[\frac{\langle(|x-x_m|-\Delta x)^2\rangle}{\langle(x-x_b)^2\rangle}\right] \quad (12)$$

   Angular brackets denote a time-series average value. Brier skill scores exceeding 0.0, 0.3, 0.6, and 0.8 are respectively classed as 'poor', 'fair', 'good' and 'excellent'.
4. The Akaike's information criterion (Akaike, 1974; Kuriyama, 2012; Davidson *et al.*, 2013a), AIC, provides an additional comparative assessment of model skill, where a penalty is incurred for the number of free parameter used, m.

$$AIC = n[\log 2\pi + 1] + n \log \sigma^2 + 2m \quad (13)$$

   n is the sample size, and σ^2 is the variance of the residuals (between validation data and the baseline or model predictions). Differences in AIC score (ΔAIC) are used to compare the models; if a model's AIC score is smaller than another model's AIC score by at least 1, it is considered more appropriate (Kuriyama, 2012).

3. Results

3.1 Description of the temporal evolution of beach three-dimensionality

Time series of α (Fig. 5) show that the lower beach contours and outer barline range in alongshore standard deviation from 5 – 30 m and 10 – 70 m, respectively. The seasonal signals (solid lines) reveal some complex annual periodicity in beach three-dimensionality. Outer bar α displays pronounced minima in winter each year (December), after which α begins to increase in the new year and usually displays a local maximum (α > 40 m) in spring between March and June. Summer is characterised by slightly lower outer bar α (20 m < α < 30 m), although 2009 and 2013 are notable exceptions, when high α (> 35 m) was maintained between March and September. The last third of each year sees a reduction in outer bar α back to its annual minimum in winter. The lower beach similarly displays reduced α in winter (annual minima in December), after which α rapidly increases (annual maxima in January/February).

Between December 2013 and February 2014 an unprecedented series of long period, high energy swell events occurred, making it the most energetic 8-week period of waves in the last 65 years (Masselink *et al.*, In press). One storm swell 'Hercules' featured wave heights and periods of 9.6 m and 22 s, respectively (Castelle *et al.*, 2015). During that stormy winter the lower beach retreated landward, and became highly three-dimensional in spring 2014. The outer bar became increasingly linear and moved offshore, but due to a subsequent lack of wave breaking over the stranded offshore bar after the storms, there are no measurements after February 2014 to indicate its recovery behaviour.

Autocorrelation of the low-pass filtered and weekly resampled α time series (Fig. 6, upper panel) reveals an annual signal at the outer bar, with significant positive and negative correlations at lags of 1 and 1.5 years, respectively. The lower beach has a sub-annual periodicity, revealed by the peaks in autocorrelation at 15 and 30 weeks lag. Cross-correlation between α at the lower beach and outer bar (Fig. 6, lower panel) reveals significant positive correlation (r ≈ 0.5) at negative lags up to 15

weeks, indicating that the lower beach becomes three-dimensional 1 – 4 months before the outer bar.

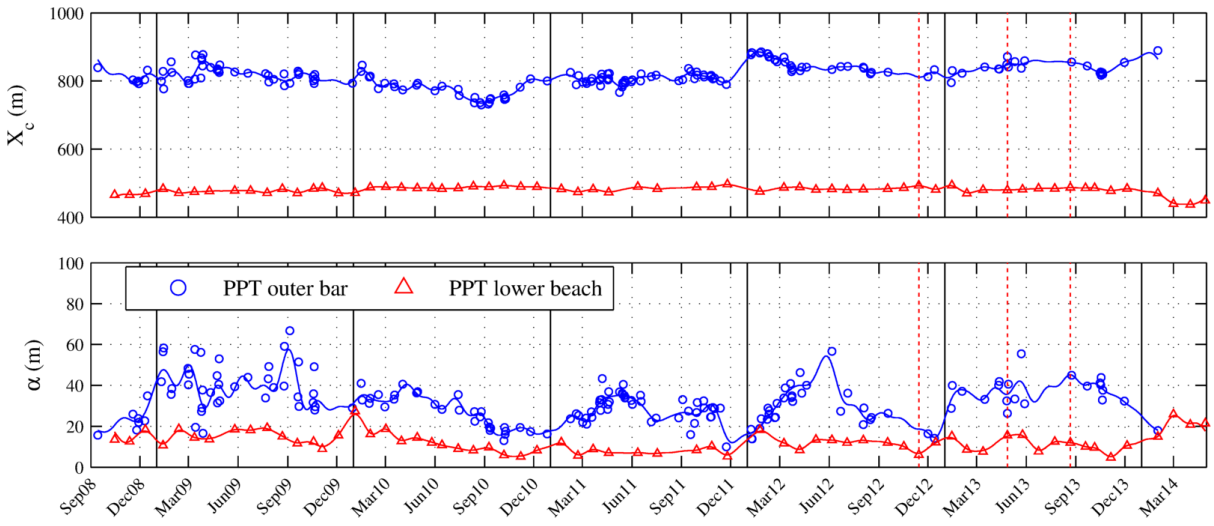

Figure 5. Time series of alongshore averaged cross-shore position, X_c, (upper) and standard deviation, α, (lower) of the outer barline and lower beach contours at Perranporth beach. The scattered points are the measured data and the associated lines are the low-pass filtered (1/42 days cut off) seasonal signal. Solid and dotted vertical lines indicate the start of each year and the measurement dates of the example data from fig. 3, respectively.

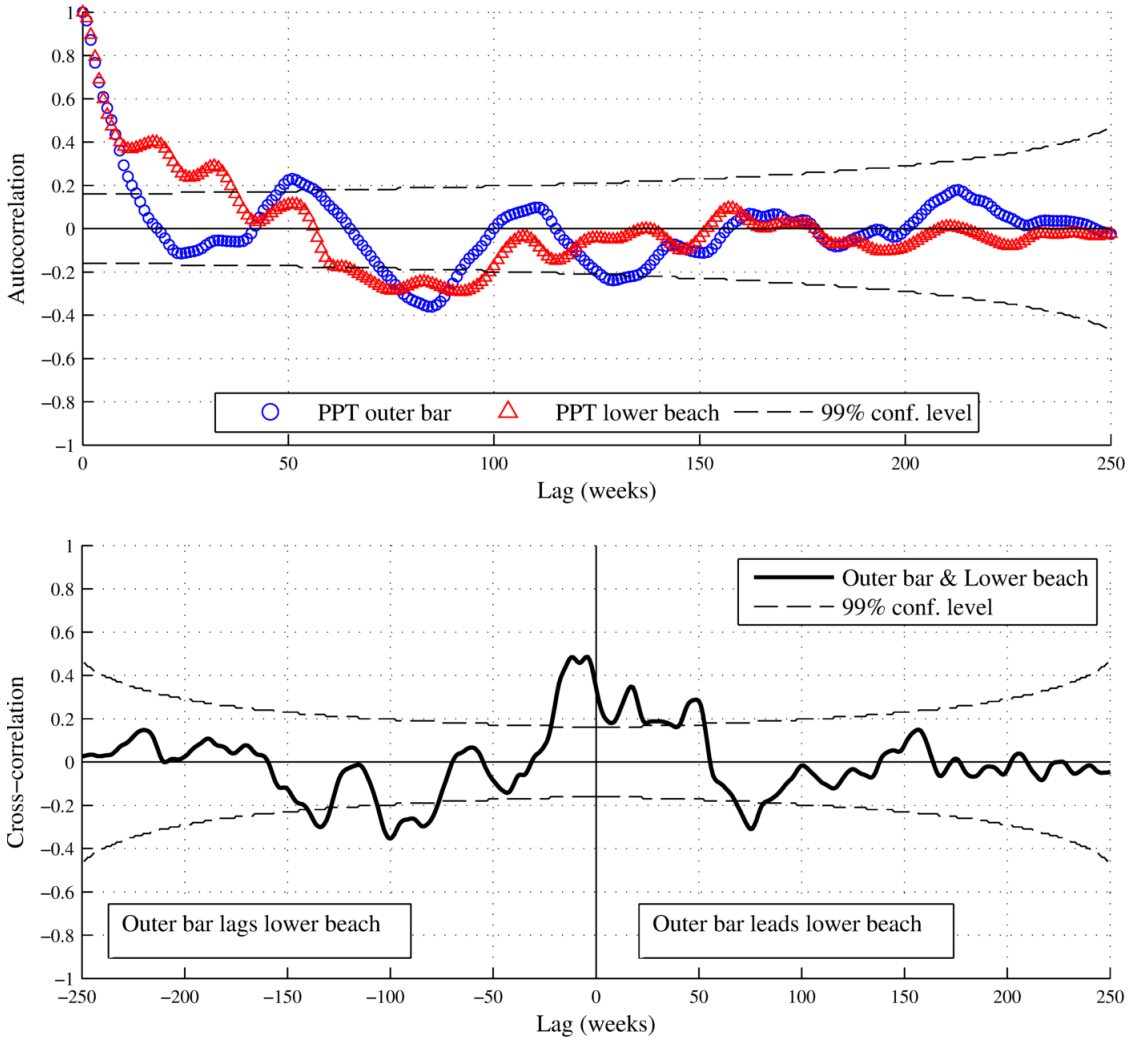

Figure 6. Upper panel: Autocorrelation function of three-dimensionality (α) at the outer bar and lower beach, at lags up to 250 weeks. Lower panel: Cross-correlation function between α at the outer bar and lower beach, at lags up to 250 weeks.

3.2 Modelling Results

3.2.1 Model Hindcast

Fig. 7 shows DST13 model hindcasts. Summary statistics (Table 1) indicate that the model performed well, explaining 42% of the variance in α at the outer bar, (RMSE = 6.55 m) and 61% of the variance in α at the lower beach (RMSE = 2.84 m). Brier Skill Scores were 'good' for both the outer bar and lower beach (0.77 and 0.63. respectively). The outer bar predictions achieved higher BSS than those at the lower beach despite the other statistics suggesting that the model performed better for the lower beach. This is due to BSS scoring sympathetically towards data with larger estimated errors (the data lines in Fig. 7 demonstrate the greater measurement error, $\Delta\alpha$, at the outer bar).

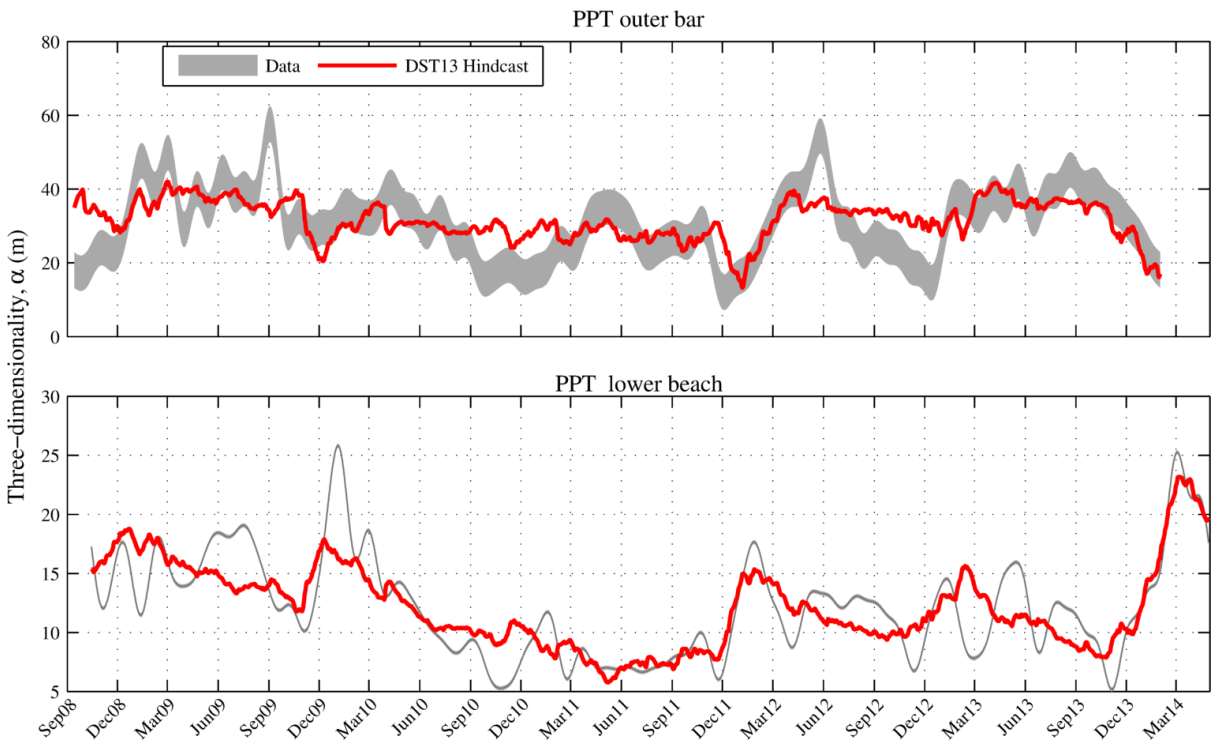

Figure 7. DST13 Model hindcasts plotted alongside the seasonal (low pass-filtered) α data at Perranporth's outer bar (upper panel) and lower beach (lower panel). The thickness of the data lines indicates the measurement error ($\Delta\alpha$).

3.2.2 Model validation

The predictive skill of the DST13 model was more rigorously tested by validating its predictions against an unseen portion of the data, as well as comparing the predictions to those made by the

PHH06 model. Both models were calibrated using the first 60% of available data, and validation was performed using the remaining unseen 40% of the data (Fig. 8). As with the hindcast, the DST13 model predicted α well at the outer bar and lower beach, explaining 57% - 59% of the variance in the validation data (RMSE = 5.9 m and 3.2 m) and achieving 'good' and 'fair' Brier Skill Scores (BSS = 0.71 and 0.53), respectively. The frequency and timing of the annual fluctuations in the lower beach data were well predicted by the model, although sub-annual signals were not well reproduced. Although the magnitude and timing of some changes at the outer bar were not accurately predicted, DST13 did predict the large increase in α between January and April 2012, and decrease in α between October 2013 and February 2014. The PHH06 model also performed well for the lower beach contour data (Fig. 8 and Table 1), explaining 61% of the variance in the data (RMSE = 3.46 m) and achieving a 'fair' Brier Skill Score (BSS = 0.46). For the outer bar the PHH06 model predicted some annual variability but the phase and amplitude of the data were not reproduced. The positive ΔAIC scores (Table 2) achieved by the DST13 model (4 free parameters) indicate that the model out-performed a linear fit to the data (2 free parameters) and the PHH06 model (8 free parameters), when the complexity of each model is taken into consideration.

DST13 model	**Free Parameters**					**Model Skill**			
						R^2	**RMSE (m)**	**BSS**	**AIC**
	a	**b**	**c**	**ϕ**	r				
PPT OB	47.5 ±3.16 (48.6 ±4.75)	−0.00718 ± 0.00212 (−0.00587 ± 0.00491)	0.00632 ± 0.00117 (0.00725 ± 0.00275)	69 (67)	0.350 (0.351)	0.417 (0.332) [0.565]	6.55 (7.21) [5.90]	0.766 'good' [0.709 'good']	1150 [440]
PPT LC	13.3 ± 1.40 (12.9 ± 2.32)	0.00300 ± 0.00148 (0.00459 ± 0.00521)	−0.00202 ± 0.000424 (−0.00240 ± 0.000877)	1000 (1000)	0.279 (0.279)	0.606 (0.634) [0.585]	2.84 (2.82) [3.22]	0.628 'good' [0.533 'fair']	324 [136]

PHH06 model	**Free Parameters**		**Model Skill**			
			R^2	**RMSE (m)**	**BSS**	**AIC**
PPT OB	$\boldsymbol{A}$	$\begin{bmatrix} -0.0000664 \pm 0.000237 & -0.000135 \pm 0.0000942 \\ -0.0145 \pm 0.00385 & -0.00157 \pm 0.00153 \end{bmatrix}$	(0.316) [0.00270]	(7.23) [10.3]	[0.155 'poor']	[527]
	$\boldsymbol{B}$	$\begin{bmatrix} 803 \pm 11.9 & 30.5 \pm 4.73 \\ 0.109 \pm 0.0371 & 0.0344 \pm 0.0148 \end{bmatrix}$				
PPT LC	$\boldsymbol{A}$	$\begin{bmatrix} -0.0000392 \pm 0.000127 & -0.000162 \pm 0.0000616 \\ 0.00448 \pm 0.00259 & -0.00106 \pm 0.00125 \end{bmatrix}$	(0.692) [0.614]	(2.58) [3.46]	[0.463 'fair']	[150]
	$\boldsymbol{B}$	$\begin{bmatrix} 470 \pm 5.47 & 12.9 \pm 2.65 \\ -0.00481 \pm 0.0132 & 0.0191 \pm 0.00640 \end{bmatrix}$				

Table 1. Model coefficients and skill assessment results for the DST13 model and PHH06 model, for the outer bar (OB) and lower beach contours (LC). Model skill values are given for hindcast, (calibration) and [validation] data; note that a hindcast was only performed with the DST13 model. Ratio r is grouped here as a parameter, but was not counted as one in the calculation of AIC. Values are given to 3 significant figures.

	ΔAIC **(Linear fit – PHH06)**	ΔAIC **(Linear fit – DST13)**	ΔAIC **(PHH06 – DST13)**
PPT OB	-22	**57**	**87**
PPT LC	**13**	**18**	**14**

Table 2. Difference in AIC scores between a linear fit to the data, the PHH06 model, and the DST13 model. Values greater than 1 (shown as bold values) indicate that the second model in parentheses is significantly better than the first.

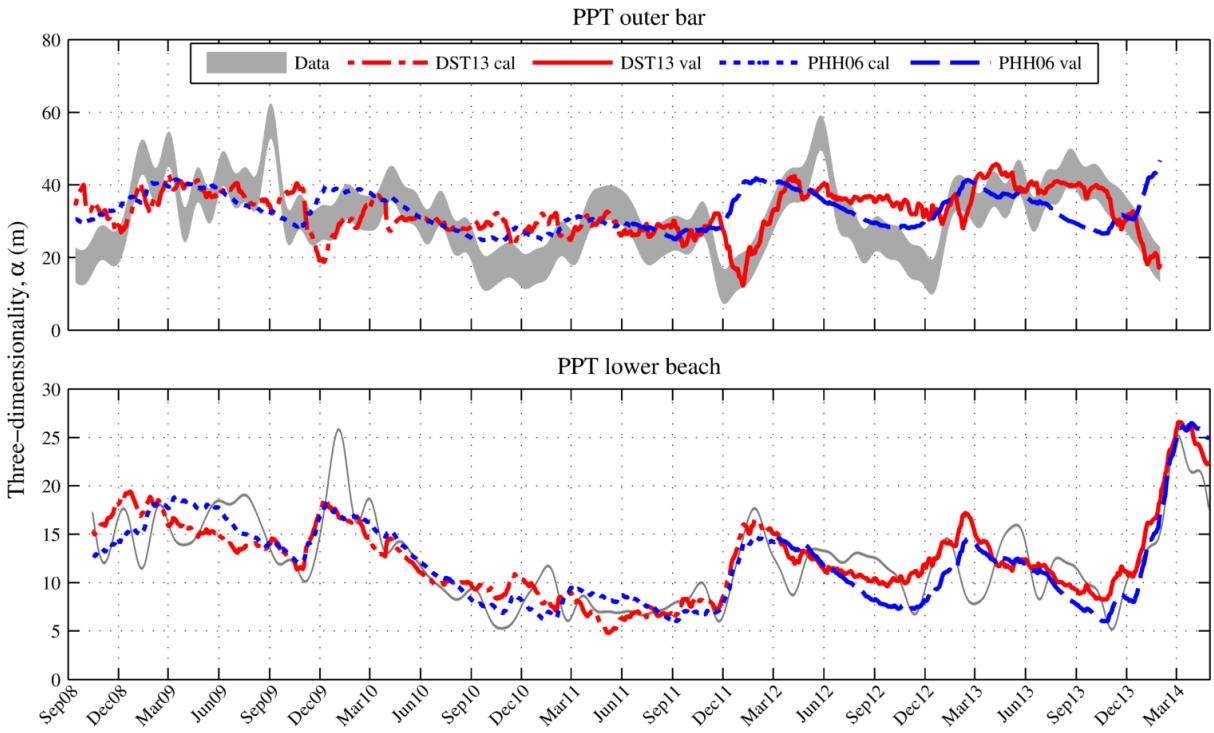

Figure 8. Calibration (cal) and validation (val) model predictions for the alongshore variability of the outer bar (upper panel) and lower beach (lower panel) at Perranporth. The thickness of the data lines indicates the measurement error.

4. Discussion

The model results indicate that disequilibrium stress is suited to modelling changes in beach three-dimensionality. It is particularly encouraging that the DST13 model performed well between December 2013 and February 2014 when an unprecedented series of long period, high energy swell events occurred. Throughout this period the model skilfully predicted three-dimensionality at the lower beach and outer bar, under wave conditions well outside the calibration data set. The time-varying equilibrium value (Ω_{eq}) in the DST13 model is a weighted function of the antecedent dimensionless fall velocity and therefore accounts for antecedent waves, but also estimates the likely state that the beach is approaching, due to the relationship between Ω and beach state (Wright and Short, 1984). As process models have shown that alongshore non-uniformities do not grow indefinitely under constant wave forcing (e.g. Smit *et al.*, 2008), the negative feedback implicitly represented in this temporally varying term maintains the stability of the system, appropriately constraining 3D growth. Allowing Ω_{eq} to vary also permits for hysteresis to occur, which is often observed as beaches change state (Lippmann and Holman, 1990; Ranasinghe *et al.*, 2004).

4.1 Comparison of the PHH06 and DST13 models

Both models predicted three-dimensionality better at the lower beach than at the outer bar, suggesting that the barline measurement error may be masking the relationship with incident waves. Despite poorly predicting outer bar α, the PHH06 model made accurate predictions of lower beach α. Unlike DST13, the PHH06 coefficients can describe positive or negative feedback depending on the results of the least squares regression. The self-interaction terms (left to right diagonal) in matrix A (Table 1) for the lower beach are both negative, showing that increases in α reduce the rate of further changes in α, suggesting a stable and deterministic system (Plant *et al.*, 2006). The fact that these terms are negative adds credence to the negative feedback approach used in the DST13

model and explains the remarkably similar predictions of lower beach α made by the two models, despite the differences in driving parameters.

The inclusion of a tidally modulated power term in DST13 may explain why it performed better than PHH06 at the outer bar, which is often inactive during small tides. While DST13 is forced by wave and tide parameters, PHH06 requires knowledge of wave height and X_c in order to predict changes in α. Plant *et al*. (2006) argue that knowledge of both X_c and α is necessary to predict either parameter, but as the DST13 model was able to predict α with significant skill, and without knowledge of X_c, this may not necessarily be the case. Fig. 9 reveals that seaward and landward lower beach contour positions that occur as the beach flattens (erodes) and steepens (accretes), are often associated with low and high three-dimensionality, respectively. This dependency may allow DST13 to predict α without explicit knowledge of X_c.

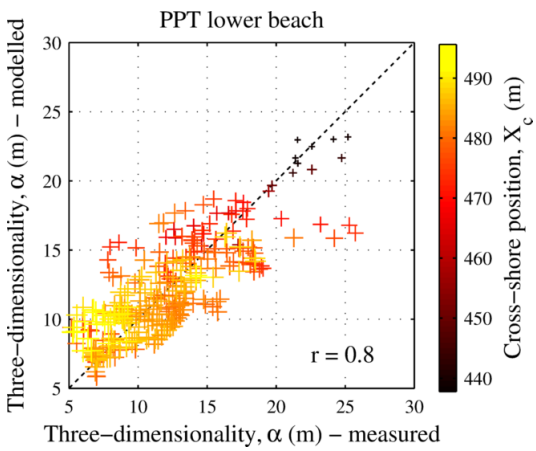

Figure 9. Measured vs modelled lower intertidal three-dimensionality, α. The measured data were low-pass filtered and resampled at weekly intervals, and the DST13 model predictions were resampled at the same instances. The size and colour of the markers represents the alongshore averaged cross-shore position of the MLWN contour, X_c, with larger markers and lighter colours showing more seaward positions. The dotted line shows a 1:1 relationship for reference.

4.2 Effect of varying memory decay length (ϕ)

Fig. 10 (upper panels) shows the effect of varying the value of ϕ on the performance and memory decay of the DST13 model. The peaks at ϕ = 67 days and ϕ >= 1000 days reveal that the memory decay for the outer bar and lower beach are more than an order of magnitude different. Fig. 10 (lower panel) further demonstrates that equilibrium conditions vary greatly over a single year at the outer bar (storm-dominated timescale), but very little at the lower beach (seasonal response). The slight peak in model performance for the lower beach at ϕ = 10 days indicates that a shorter response may also occur there, but data with a higher temporal resolution would be needed to investigate this further. Interestingly, the peak ϕ value for the outer bar is associated with a drop in model skill at the lower beach (Fig. 10, upper left panel). This is likely to be due to the lagged behaviour of the outer bar, which was previously shown to reach peak values of α up to 15 weeks after the lower beach (Fig. 6). Because high α at the lower beach can occur alongside low α at the outer bar (Fig. 5), a model suited to predicting one (i.e. with ϕ = 67 days) is likely to perform poorly for the other.

This lag also results in rate coefficients (c) with opposing signs at the outer bar and lower beach. As the outer bar becomes 3D weeks to months after annual peak wave conditions, the increase in α coincides with positive $\Delta\Omega$, yielding a positive c term. Conversely at the lower beach three-dimensionality begins to increase immediately following the annual peak wave conditions while $\Delta\Omega$ is decreasing but still negative, and therefore yields a negative c term. The lagged increase in α at the outer bar relative to the lower beach raises questions about whether 3D features formed at the lower beach influence or initiate the bed-surf coupling required to develop 3D features at the bars, but this question cannot be answered with the present data alone.

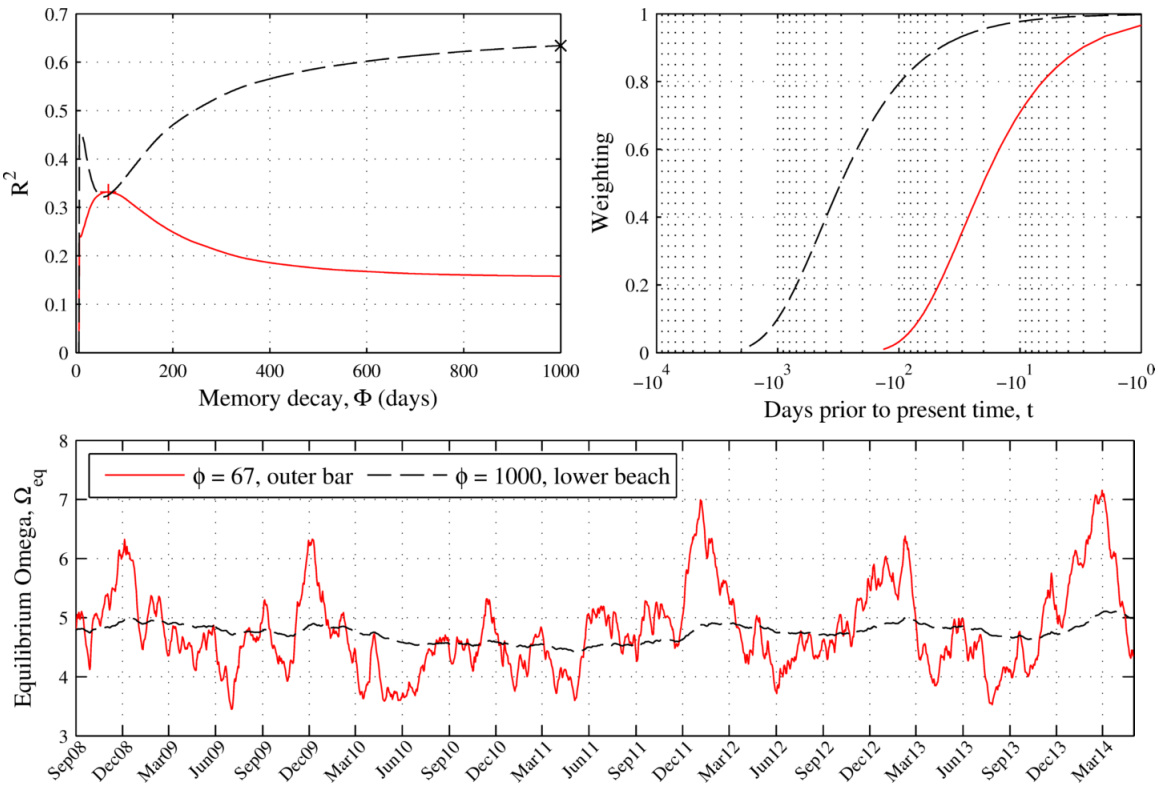

Figure 10. Upper left panel: Model sensitivity to the value of ϕ for the outer bar (solid line) and lower beach (dashed line). The ϕ associated with the largest calibration R^2 was chosen as the optimal value for each data set, denoted as a cross (ϕ = 67) and an x (ϕ = 1000). Upper right panel: example of memory decay used to determine the weighted-average antecedent wave conditions for ϕ = 67 (solid line) and ϕ = 1000 (dashed line). Note the x axis is logarithmic. Lower panel: Time series of Ω_{eq} over the period of interest for the outer bar (solid line) and lower beach (dashed line).

4.3 Model limitations and improvements

Although processes are not explicitly modelled, DST13 assumes changes in three-dimensionality occur as a result of normal, open beach circulation. For example the model presently ignores the effects of alongshore oriented wave power, which idealised modelling (Ranasinghe *et al.*, 2004; Splinter *et al.*, 2011; Garnier *et al.*, 2013; Price *et al.*, 2013) and field studies (Holman *et al.*, 2006; Thornton *et al.*, 2007; Price *et al.*, 2011; Price *et al.*, 2013) have shown to be an important cause of sandbar straightening at some sites. It is proposed that this could be accounted for simply in the model by incorporating the absolute value of the alongshore component of wave power $|P_y|$, either

as an additional model parameter at the cost of one extra regression term, or by incorporating it into forcing term F. When tested, this altered the model results very little due to the small contribution of obliquely incident waves at Perranporth, where alongshore-oriented power is typically an order of magnitude smaller than the total wave power. This modification was therefore not included in the present model, but provides a basis for further model development at sites with significant alongshore wave power.

As the degree of three-dimensionality at dissipative-intermediate sites (such as Perranporth) is inversely related to Ω (Wright and Short, 1984), Ω_{eq} provides a suitable equilibrium value for three-dimensionality. However, beaches that transition from the TBR to LTT states and eventually to the R end state, feature decreasing three-dimensionality as Ω decreases. Therefore in order to generalise the model to sites that feature intermediate-reflective beach states the model would need to be adapted, such that when Ω_{eq} exceeds an appropriate threshold the sign of the disequilibrium is inverted. At that point increases in Ω would change from driving an increase in α to driving a decrease in α.

The improvements achieved at the outer bar by moderating the wave power based on the tidal range reflect the fact that significant sediment transport can only occur under sufficient wave breaking (Splinter *et al.*, 2011). A large tide range reduces the water depth over the outer bar at low tide, and therefore increases breaking and sediment transport which enhances the rate of change in the bar. Conversely under neap tides, when water depth over the bar is large relative to the wave height, sediment transport (and therefore changes in the bar) can significantly reduce due to the lack of breaking. These processes may also explain the storm-dominated timescale of the outer bar response, as a previously inactive bar can rapidly change when larger storm waves break. Although the tidally modulated wave power term reduces the rate of morphological change under small tides and waves, completely reducing bar change to zero when the subtidal bar is inactive may yield further improvements.

5. Conclusions

A dataset of 5.5 years of quasi-daily bar measurements, and quasi-monthly intertidal beach surveys from Perranporth beach (Cornwall, UK) were used to quantify seasonal to inter-annual changes in beach three-dimensionality (α). α at the outer bar displayed significant annual periodicity, with annual minima and maxima occurring in winter and spring respectively. The lower intertidal beach displayed a similar periodicity, but developed three-dimensionality 1-4 months before the outer bar. A simple equilibrium model (DST13) was developed, which made skilful hindcast and calibration-validation predictions of α, explaining 42% and 61% of the variability in outer bar and lower beach three-dimensionality, respectively. The model was able to make skilful predictions during an unprecedented series of long period, high energy swell events, including the most energetic 8-week period of waves measured in the last 65 years (December 2013 to February 2014), which were outside the training data range.

At present the model assumes that open beach, cross-shore processes, such as horizontal wave-driven circulation control the morphodynamics, but alongshore-oriented wave power should be considered at sites where it is significant relative to the normally oriented power. Negative feedback was found to be an important process governing the changes in beach three-dimensionality. While free morphological behaviour may drive three-dimensional growth, negative feedback processes exert stability in the system, making it inherently predictable using a temporally varying equilibrium value, as used here. In its present form the model out-performed a simple baseline model (a linear fit) as well as a comparable linearized feedback model from the literature (Plant *et al.*, 2006), providing the first long-term (multi-year) predictions of seasonal to inter-annual beach three-dimensionality for a macrotidal beach.

Acknowledgements

We would like to thank Martin Austin, Tim Poate, Tim Scott, Erwin Bergsma and Sam Prodger for their hard work in collecting much of the survey data. Thanks also go to Peter Ganderton and Megan Sheridan for technical support. We would also like to thank the NERC DRIBS project (code: NE/HOO4262/1), the EU SOWFIA project, and the Plymouth University Marine Institute for funding the beach surveys.

References

Akaike, H., 1974. A new look at the statistical model identification. Automatic Control, IEEE Transactions on, 19(6), 716-723.

Almar, R., Castelle, B., Ruessink, B., Sénéchal, N., Bonneton, P., Marieu, V., 2010. Two-and three-dimensional double-sandbar system behaviour under intense wave forcing and a meso–macro tidal range. Continental Shelf Research, 30(7), 781-792.

Austin, M., Scott, T., Brown, J., MacMahan, J., Masselink, G., Russell, P., 2010. Temporal observations of rip current circulation on a macrotidal beach. Continental Shelf Research, 30(9), 1149-1165.

Austin, M.J., Scott, T.M., Russell, P.E., Masselink, G., 2013. Rip current prediction: Development, validation, and evaluation of an operational tool. Journal of Coastal Research, 29(2), 283-300.

Bowen, A.J., 1969. Rip currents: 1. Theoretical investigations. Journal of Geophysical research, 74(23), 5467-5478.

Brighton, B., Sherker, S., Brander, R., Thompson, M., Bradstreet, A., 2013. Rip current related drowning deaths and rescues in Australia 2004–2011. Natural Hazards and Earth System Science, 13(4), 1069-1075.

Caballeria, M., Calvete, D., Coco, G., Dodd, N., Falques, A., 2003a. Formation and alongshore spacing of crescentic bars, The 3rd Symposium on River, Coastal and Estuarine Morphodynamics. Int. Assoc. for Hydraul. Res., Delft.

Caballeria, M., Coco, G., Falques, A., 2003b. Crescentic patterns and self-organization processes on barred beaches, Coastal Sediments. Am. Soc. of Civ. Eng., New York.

Caballeria, M., Coco, G., Falqués, A., Huntley, D., 2002. Self-organization mechanisms for the formation of nearshore crescentic and transverse sand bars. Journal of Fluid Mechanics, 465, 379-410.

Castelle, B., Bonneton, P., Dupuis, H., Sénéchal, N., 2007. Double bar beach dynamics on the high-energy meso-macrotidal French Aquitanian Coast: A review. Marine Geology, 245(1–4), 141-159.

Castelle, B., Coco, G., 2012. The morphodynamics of rip channels on embayed beaches. Continental Shelf Research, 43, 10-23.

Castelle, B., Marieu, V., Bujan, S., Ferreira, S., Parisot, J.-P., Capo, S., Sénéchal, N., Chouzenoux, T., 2014. Equilibrium shoreline modelling of a high-energy meso-macrotidal multiple-barred beach. Marine Geology, 347, 85-94.

Castelle, B., Marieu, V., Bujan, S., Splinter, K.D., Robinet, A., Sénéchal, N., Ferreira, S., 2015. Impact of the winter 2013–2014 series of severe Western Europe storms on a double-barred sandy coast: Beach and dune erosion and megacusp embayments. Geomorphology, 238, 135-148.

Davidson, M., Huntley, D., Holman, R., George, K., 1997. The evaluation of large scale (km) intertidal beach morphology on a macrotidal beach using video images, Coastal Dynamics. ASCE, pp. 385-394.

Davidson, M., Lewis, R., Turner, I., 2010. Forecasting seasonal to multi-year shoreline change. Coastal Engineering, 57(6), 620-629.

Davidson, M., Splinter, K., Turner, I., 2013a. A simple equilibrium model for predicting shoreline change. Coastal Engineering, 73, 191-202.

Davidson, M.A., Turner, I.L., Splinter, K.D., 2013b. Predicting Shoreline Response to Cross-Shore Processes in a Changing Wave Climate, Coastal Dynamics, Arcachon, France.

Dean, R.G., 1973. Heuristic models of sand transport in the surf zone, First Australian Conference on Coastal Engineering: Engineering Dynamics of the Coastal Zone. Institution of Engineers, Australia, pp. 215.

Falqués, A., Coco, G., Huntley, D., 2000. A mechanism for the generation of wave-driven rhythmic patterns in the surf zone. Journal of Geophysical Research: Oceans (1978–2012), 105(C10), 24071-24087.

Falqués, A., Dodd, N., Garnier, R., Ribas, F., MacHardy, L.C., Larroudé, P., Calvete, D., Sancho, F., 2008. Rhythmic surf zone bars and morphodynamic self-organization. Coastal Engineering, 55(7–8), 622-641.

Garnier, R., Falqués, A., Calvete, D., Thiebot, J., Ribas, F., 2013. A mechanism for sandbar straightening by oblique wave incidence. Geophysical Research Letters, 40(11), 2726-2730.

Gourlay, M., 1968. Beach and dune erosion tests. Delft Hydraulics Laboratory, Report M, 935.

Holman, R.A., Symonds, G., Thornton, E.B., Ranasinghe, R., 2006. Rip spacing and persistence on an embayed beach. Journal of Geophysical Research: Oceans (1978–2012), 111(C1).

Kingston, K., Ruessink, B., Van Enckevort, I., Davidson, M., 2000. Artificial neural network correction of remotely sensed sandbar location. Marine Geology, 169(1), 137-160.

Kuriyama, Y., 2012. Process-based one-dimensional model for cyclic longshore bar evolution. Coastal Engineering, 62, 48-61.

Larson, M., Hoan, L.X., Hanson, H., 2010. Direct formula to compute wave height and angle at incipient breaking. Journal of waterway, port, coastal, and ocean engineering, 136(2), 119-122.

Lippmann, T., Holman, R., 1990. The spatial and temporal variability of sand bar morphology. Journal of Geophysical Research, 95, 11575-11590.

Lippmann, T., Holman, R.A., 1989. Quantification of sand bar morphology: A video technique based on wave dissipation. Journal of Geophysical Research: Oceans (1978–2012), 94(C1), 995-1011.

Loureiro, C., Ferreira, Ó., Cooper, J.A.G., 2012. Geologically constrained morphological variability and boundary effects on embayed beaches. Marine Geology, 329–331, 1-15.

MacMahan, J., Reniers, A., Brown, J., Brander, R., Thornton, E., Stanton, T., Brown, J., Carey, W., 2011. An introduction to rip currents based on field observations. Journal of Coastal Research, 27(4), 3-6.

MacMahan, J.H., Thornton, E.B., Reniers, A.J., 2006. Rip current review. Coastal Engineering, 53(2), 191-208.

Masselink, G., Austin, M., Scott, T., Poate, T., Russell, P., 2014. Role of wave forcing, storms and NAO in outer bar dynamics on a high-energy, macro-tidal beach. Geomorphology, 226, 76-93.

Masselink, G., Hegge, B., 1995. Morphodynamics of meso-and macrotidal beaches: examples from central Queensland, Australia. Marine Geology, 129(1), 1-23.

Masselink, G., Scott, T., Conley, D.C., Davidson, M., Russell, P., In press. Regional Variability in Atlantic Storm Response Along the SouthWest Coast of England, Coastal Sediments 2015, San Diego, CA, USA.

Masselink, G., Short, A.D., 1993. The effect of tide range on beach morphodynamics and morphology: a conceptual beach model. Journal of Coastal Research, 9(3), 785-800.

Mead, S., Black, K., 2001a. Field studies leading to the bathymetric classification of world-class surfing breaks. Journal of Coastal Research(SI 29), 5-20.

Mead, S., Black, K., 2001b. Functional component combinations controlling surfing wave quality at world-class surfing breaks. Journal of Coastal Research(SI 29), 21-32.

Morris, B.D., Davidson, M.A., Huntley, D.A., 2001. Measurements of the response of a coastal inlet using video monitoring techniques. Marine Geology, 175(1), 251-272.

Pape, L., Ruessink, B.G., Wiering, M.A., Turner, I.L., 2007. Recurrent neural network modeling of nearshore sandbar behavior. Neural Networks, 20(4), 509-518.

Plant, N.G., Holland, K.T., Puleo, J.A., 2002. Analysis of the scale of errors in nearshore bathymetric data. Marine Geology, 191(1-2), 71-86.

Plant, N.G., Holman, R.A., Freilich, M.H., Birkemeier, W., 1999. A simple model for interannual sandbar behavior. Journal of Geophysical Research: Oceans (1978–2012), 104(C7), 15755-15776.

Plant, N.G., Todd Holland, K., Holman, R.A., 2006. A dynamical attractor governs beach response to storms. Geophysical Research Letters, 33(17).

Poate, T., Masselink, G., Russell, P., Austin, M., 2014. Morphodynamic variability of high-energy macrotidal beaches, Cornwall, UK. Marine Geology, 350, 97-111.

Poate, T.G., 2011. Morphological Response of High Energy Macrotidal Beaches. Doctor of Philosophy Ph.D. thesis, Plymouth University, Plymouth, 255 pp.

Price, T., Ruessink, B., Castelle, B., 2014. Morphological coupling in multiple sandbar systems–a review. Earth Surface Dynamics, 2, 309-321.

Price, T., Rutten, J., Ruessink, B., 2011. Coupled behaviour within a double sandbar system. Journal of Coastal Research(SI 64), 125-129.

Price, T.D., Ruessink, B., Castelle, B., 2013. Morphological coupling in a double sandbar systemPh.D. thesis, Utrecht University.

Ranasinghe, R., Symonds, G., Black, K., Holman, R., 2004. Morphodynamics of intermediate beaches: a video imaging and numerical modelling study. Coastal Engineering, 51(7), 629-655.

Ruessink, G., Price, T., Castelle, B., 2013. Finite-Amplitude Behaviour of alongshore variability in nearshore sandbars: observations and modelling, Coastal Dynamics, pp. 1-15.

Scarfe, B.E., Healy, T.R., Rennie, H.G., 2009. Research-based surfing literature for coastal management and the science of surfing-a review. Journal of Coastal Research, 25(3), 539-557.

Scott, T., Masselink, G., Russell, P., 2011. Morphodynamic characteristics and classification of beaches in England and Wales. Marine Geology, 286(1-4), 1-20.

Scott, T., Russell, P., Masselink, G., Wooler, A., Short, A., 2008. High volume sediment transport and its implications for recreational beach risk, Proceedings 31st International Conference on Coastal Engineering. ASCE, Hamburg, Germany, pp. 4250-4262.

Short, A., 1991. Macro-meso tidal beach morphodynamics: An overview. Journal of Coastal Research, 7, 417-436.

Short, A.D., 1979. Wave power and beach-stages: a global model, Proc. 16th Int. Conf. Coastal Engineering, Hamburg, pp. 1145-1162.

Short, A.D., 1992. Beach systems of the central Netherlands coast: processes, morphology and structural impacts in a storm driven multi-bar system. Marine Geology, 107(1), 103-137.

Short, A.D., 1996. The role of wave height, period, slope, tide range and embaymentisation in beach classifications: a review. Revista Chilena de Historia Natural, 69(4), 589-604.

Short, A.D., Aagaard, T., 1993. Single and multi-bar beach change models. Journal of Coastal Research, 141-157.

Smit, M., Reniers, A., Ruessink, B., Roelvink, J., 2008. The morphological response of a nearshore double sandbar system to constant wave forcing. Coastal Engineering, 55(10), 761-770.

Splinter, K.D., Holman, R.A., Plant, N.G., 2011. A behavior-oriented dynamic model for sandbar migration and 2DH evolution. Journal of Geophysical Research: Oceans (1978–2012), 116(C1).

Splinter, K.D., Turner, I.L., Davidson, M.A., Barnard, P., Castelle, B., Oltman-Shay, J., 2014. A generalized equilibrium model for predicting daily to interannual shoreline response. Journal of Geophysical Research: Earth Surface, 119(9), 1936-1958.

Sutherland, J., Peet, A., Soulsby, R., 2004. Evaluating the performance of morphological models. Coastal Engineering, 51(8), 917-939.

Sverdrup, H.U., Munk, W.H., 1946. Theoretical and empirical relations in forecasting breakers and surf. Transactions, American Geophysical Union, 27, 828-836.

Thornton, E.B., MacMahan, J., Sallenger Jr, A., 2007. Rip currents, mega-cusps, and eroding dunes. Marine Geology, 240(1), 151-167.

Van de Lageweg, W., Bryan, K.R., Coco, G., Ruessink, B., 2013. Observations of shoreline–sandbar coupling on an embayed beach. Marine Geology, 344, 101-114.

Van Enckevort, I., Ruessink, B., 2001. Effect of hydrodynamics and bathymetry on video estimates of nearshore sandbar position. Journal of Geophysical Research: Oceans (1978–2012), 106(C8), 16969-16979.

Van Enckevort, I., Ruessink, B., Coco, G., Suzuki, K., Turner, I., Plant, N.G., Holman, R.A., 2004. Observations of nearshore crescentic sandbars. Journal of Geophysical Research: Oceans (1978–2012), 109(C6).

Wright, L., Short, A., Green, M., 1985. Short-term changes in the morphodynamic states of beaches and surf zones: an empirical predictive model. Marine Geology, 62(3), 339-364.

Wright, L.D., Short, A.D., 1984. Morphodynamic variability of surf zones and beaches: A synthesis. Marine Geology, 56(1–4), 93-118.

Yates, M., Guza, R., O'Reilly, W., 2009. Equilibrium shoreline response: Observations and modeling. Journal of Geophysical Research: Oceans (1978–2012), 114(C9).

Yates, M., Guza, R., O'Reilly, W., Hansen, J., Barnard, P., 2011. Equilibrium shoreline response of a high wave energy beach. Journal of Geophysical Research: Oceans (1978–2012), 116(C4).